



Full Length Article

Ground state structure and physical properties of silicon monoxide sheet

Yanyan Chen, Yupeng Shen, Yiheng Shen, Xiaoyin Li, Yaguang Guo, Qian Wang*

Center for Applied Physics and Technology, Department of Materials Science and Engineering, HEDPS, BKL-MEMD, College of Engineering, Peking University, Beijing 100871, China

ARTICLE INFO

Keywords:

2D silicon monoxide (SiO)

Global structure search

Physical properties

Ground state structure

ABSTRACT

Two-dimensional (2D) silicon oxides have received considerable attention in recent years because of their excellent compatibility with the well-developed Si-based semiconductor technology. Though the ground state structure of 2D silicon dioxide (SiO₂) was identified many years ago, the corresponding study of 2D silicon monoxide (SiO) has not yet been reported. Herein, using global structure search method combined with density functional theory and Boltzmann transport theory, we find the ground state structure of 2D SiO, named Orth-SiO, and systematically study its physical properties. Orth-SiO is found to be thermally, dynamically and mechanically stable, and possesses a direct band gap of 1.52 eV, which is much smaller as compared to that of α -2D silica (7.31 eV). Moreover, it exhibits significant anisotropies in mechanical properties and optical adsorption due to its exceptional atomic configuration. The lattice thermal conductivity of Orth-SiO is 80.45 and 33.79 W/mK along the x and y directions at room temperature, respectively, much higher than that of many Si-based materials due to its weak anharmonicity. In addition, the carrier mobility is $8.5 \times 10^3 \text{ cm}^2 \text{ V}^{-1} \text{ s}^{-1}$, much greater than that of many other oxides. These results add new features to silicon oxides family.

1. Introduction

Silicon monoxide (SiO), which possesses high interstellar abundance, is the most common oxide of silicon in the universe [1]. The widely used method of synthesizing SiO is heating silicon dioxide with silicon [2], although many other methods for preparing high-purity SiO have also been proposed [3,4]. Due to its mature preparation techniques, wide band gap and low refractive index, the commercial SiO is widely used as the protective film of optical fibers and dielectric material of capacitors [5–7]. However, most of the commercial SiO are in amorphous phase where the conventional diffraction methods, such as X-ray diffraction, X-ray Raman scattering, small-angle X-ray scattering, cannot provide detailed information on their structures [8]. Therefore, there is no assured conclusion about the structure of SiO [9,10]. Moreover, the amorphous SiO is metastable and will decompose to Si and SiO₂ under certain conditions [6,11,12]. So, it is highly desirable to identify the possible crystalline structures of 3D and 2D SiO [10,13,14]. Mankefors *et al.* predicted the probable structures of 3D SiO by element substitution in known crystal structures, including rock salt, zinc blende, wurtzite and SnO [13]. Subsequently, AlKaabi *et al.* explored the ground state structures of 3D SiO at 1 atm and high pressures up to 200 GPa through the evolutionary and random structure searches [10], and found that the ground state structure of 3D SiO is a semiconductor

while the high pressure SiO phases are metallic.

However, when going from 3D to 2D, to the best of our knowledge, the ground state structure of 2D SiO has not yet been identified. To date, only three possible structures of 2D SiO, namely ep-sSiO, a-sSiO and z-sSiO have been reported [14]. This motivates us to explore the ground state structure of 2D SiO and study its properties by using the particle swarm optimization (PSO) algorithm combined with first principles calculations. Parallel to the expansion from 3D SiO₂ to 3D SiO, our study expands the low-dimensional silicon oxide family from 2D SiO₂ to 2D SiO, providing new understandings on how the geometry and properties of silicon oxides change with the dimensionality and oxygen concentration, which are helpful for experimentalists to tune the structure and properties by changing oxygen concentration.

2. Computational methods

The ground state of 2D SiO sheet is predicted by using the particle swarm optimization (PSO) algorithm implemented in the Crystal structure AnaLYsis by Particle Swarm Optimization (CALYPSO) package [15,16]. The population size and the number of generations are set to thirty and fifty, respectively, to ensure the convergence. Considering the fact that silicon atom prefers to form a tetrahedral configuration and the experimental thickness of 2D hexagonal silica is

* Corresponding author.

E-mail address: qianwang2@pku.edu.cn (Q. Wang).

4.34 Å [17,18], the buffering thickness is set as 4.5 Å to accommodate the buckling of structure. The vacuum space of 16 Å is included to avoid the interaction from its periodic images.

The geometric optimization and calculations of electronic structure are performed using density functional theory (DFT) as included in the Vienna *ab initio* Simulation Package (VASP) [19]. The interactions between ion cores and valence electrons are described within the projector augmented wave (PAW) method [20,21] with the kinetic energy cutoff of 500 eV. The electron exchange-correlation interaction is treated by the Perdew-Burke-Ernzerhof (PBE) functional [22] within the generalized gradient approximation (GGA) [23]. To obtain the accurate electronic band structure, we recalculate the band structure with the hybrid functional of Heyd-Scuseria-Ernzerhof (HSE06) [24,25]. The first Brillouin zone is represented by using the Monkhorst-Pack scheme [26] with a grid density of $2\pi \times 0.02 \text{ \AA}^{-1}$. The convergence criteria for total energy and atomic force components are set to 10^{-8} eV and 10^{-6} eV/Å, respectively. The thermal stability is examined by using *ab initio* molecular dynamics (AIMD) simulation.

The calculation of lattice thermal conductivity is based on the semi-classical phonon Boltzmann transport equation (BTE) [27] as implemented in ShengBTE code [28], where the required harmonic second-order interatomic force constants (IFCs) and the anharmonic third-order IFCs are calculated using the Phonopy package [29]. To balance both the calculation accuracy and computational cost, the 7th nearest neighbors are considered. The phonon dispersion is obtained with the finite displacement method [30] and the specific heat capacity is further calculated using the second-order IFCs.

3. Results and discussion

3.1. Geometric structure and stability

By performing the global structure search for 2D SiO, we obtain the energetically most stable configuration, namely, the ground state structure of 2D SiO, as displayed in Fig. 1. This structure belongs to Cmma space group (No. 67) and has an orthogonal unit cell with eight Si atoms and eight O atoms, so we name it Orth-SiO. The optimized lattice constants are $a = 5.50 \text{ \AA}$ and $b = 6.91 \text{ \AA}$, and the side view shows that Orth-SiO possesses a finite thickness of 3.60 Å. The Si atoms occupy the Wyckoff position of 8 m (0.5000, 0.0749, 0.4450) and the O atoms occupy the Wyckoff position of 8 l (0.2500, 0.0000, 0.4053). Each Si atom is connected with two Si atoms and two O atoms, forming a tetrahedral configuration, and all oxygen atoms are bonded to two Si

Table 1

Relative energy ΔE (in eV/atom) with respect to the lowest energy structure, lattice parameters (in Å), Si-Si and Si-O bond lengths (in Å) of Orth-SiO, z-sSiO, a-sSiO and ep-sSiO.

2D SiO allotropes	ΔE	a	b	$d_{\text{Si-Si}}$	$d_{\text{Si-O}}$
Orth-SiO	0.000	5.50	6.91	2.41	1.67
z-sSiO	0.047	4.04	2.81	2.41	1.68
		(4.04)	(2.71)	(2.41)	(1.68)
a-sSiO	0.061	7.06	2.80	2.40, 2.43	1.68
		(7.08)	(2.81)	(2.40, 2.43)	(1.68)
ep-sSiO	0.212	7.42	4.02	2.40	1.70
		(7.40)	(4.06)	(2.41)	(1.70)

*The numbers in parentheses are from Ref. [14].

atoms.

It is worth mentioning that the previously proposed z-sSiO, a-sSiO and ep-sSiO [14] are also obtained as the metastable SiO phases during the structure search process. This verifies the accuracy and effectiveness of the structure search method. We list their relative energies with respect to the lowest energy structure (Orth-SiO), the lattice parameters, and the Si-O and Si-Si bond lengths in Table 1 for comparison. One can see that the average Si-Si bond length of Orth-SiO is comparable to that of other three SiO allotropes, while the average Si-O bond length is slightly shorter, leading to the lower energy of Orth-SiO. We also note that the Si-Si bond length of 2.41 Å in Orth-SiO is larger than that of low-buckled silicene (2.28 Å) [31] and diamond-Si (2.37 Å) [10], showing a single bond character. While the Si-O bond length of 1.67 Å is larger than the value of 1.63 Å in the ground state structure of 2D SiO₂ (α -2D silica) [32].

We then examine the dynamic stability of Orth-SiO by calculating its phonon spectra. Fig. 2(a) displays the phonon dispersion along the high-symmetry paths of the first Brillouin zone. One can see that all the frequencies of vibrational modes are positive, confirming that Orth-SiO is dynamically stable. In addition, we notice that the highest frequency of Orth-SiO at the Γ point reaches 28 THz, which is higher than that of z-sSiO, a-sSiO and ep-sSiO (about 25 THz) [14], implying the stronger bonding and better energetics [33].

The thermal stability of Orth-SiO is studied by performing AIMD simulation using a $4 \times 3 \times 1$ supercell and the canonical (NVT) ensemble at different temperatures from 300 to 1000 K. The simulation time is 10 picoseconds (ps) with a time step of 2 femtoseconds (fs) for the each simulation. The results at 1000 K are plotted in Fig. 2(b). One can see that during the entire simulation, Orth-SiO does not suffer from

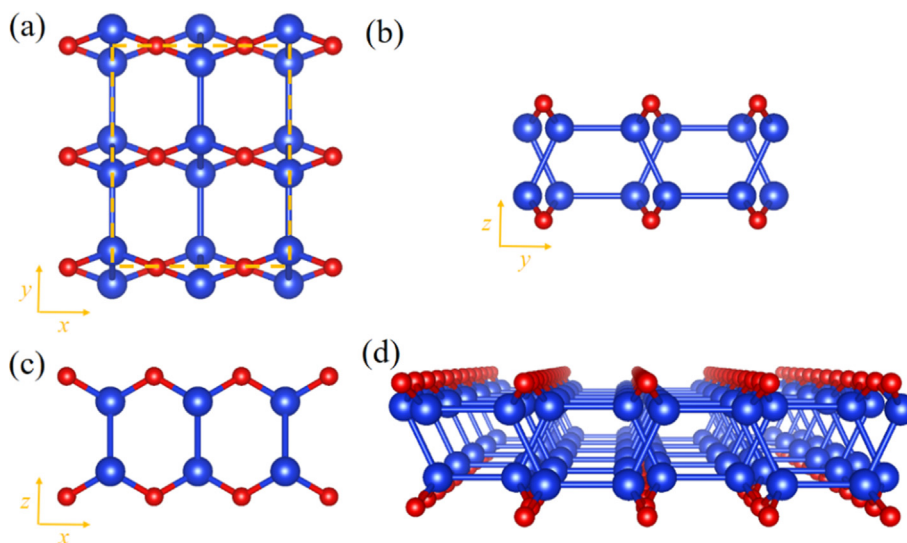


Fig. 1. Different views of the geometric structure of Orth-SiO along the (a) z, (b) x and (c) y directions, and (d) perspective view. Blue and red spheres stand for Si and O atoms, respectively. (For interpretation of the references to colour in this figure legend, the reader is referred to the web version of this article.)

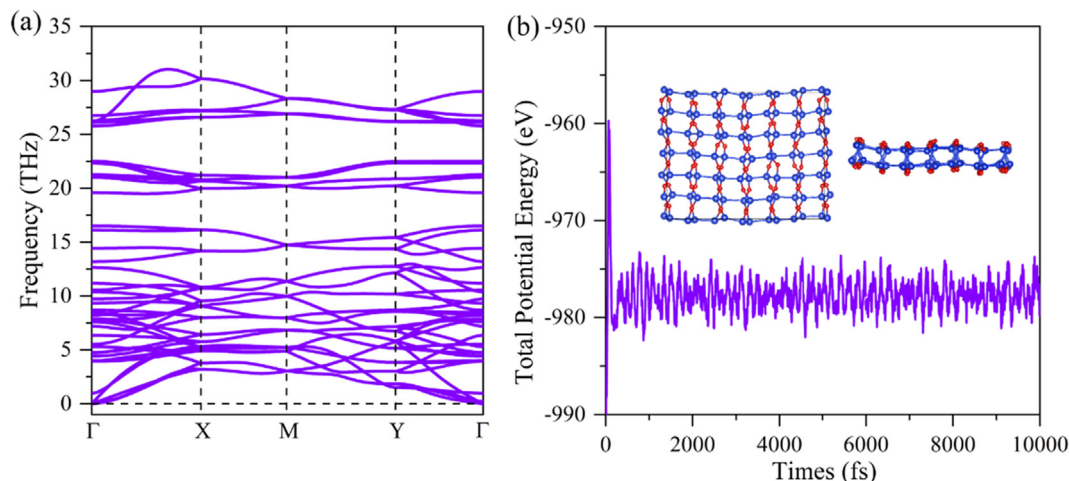


Fig. 2. (a) Phonon dispersion of Orth-SiO. (b) Potential energy fluctuation of Orth-SiO during AIMD simulation at 1000 K. The insets show the snapshot at the end of simulation.

drastic structural distortion or transformation, and the total potential energy only fluctuates around a constant value, which demonstrates that Orth-SiO is thermally stable and can tolerate temperature up to 1000 K. The snapshot of structure at the end of the simulation is illustrated in Fig. 2(b).

Next we examine the mechanical stability of Orth-SiO. In the linear elastic range, the elastic constant tensors form a 6×6 matrix with 21 independent components. For a 2D orthorhombic phase, only C_{11} , C_{12} , C_{22} , C_{44} are independent [34]. According to Born-Huang criteria [35], if a 2D orthorhombic structure is mechanically stable, the corresponding elastic constants have to satisfy $C_{11} > 0$, $C_{22} > 0$, $C_{44} > 0$, $C_{11}C_{22} - C_{12}^2 > 0$. For Orth-SiO, the four independent elastic constant components are $C_{11} = 136.84$ N/m, $C_{22} = 80.41$ N/m, $C_{44} = 20.48$ N/m and $C_{12} = 26.69$ N/m, confirming the mechanical stability.

After verifying the stability of Orth-SiO, we explore the possible synthesizing method. Here, we propose a possible procedure for synthesizing Orth-SiO, as shown in Fig. 3. We first use the low-buckled honeycomb silicene to construct a two-layered silicon structure by AA-stacking, then we introduce oxygen atoms on the bridges sites forming Si-O-Si bonds as observed in silicene oxides [36–38]. After full optimization, this configuration changes to Orth-SiO, suggesting that it is

possible to synthesize Orth-SiO by partially oxidizing bilayer silicene in experiment.

3.2. Mechanical properties

The in-plane Young's moduli E_a and E_b along the (1 0 0) and (0 1 0) directions are calculated by using equations of $E_a = (C_{11}^2 - C_{12}^2)/C_{11}$ and $E_b = (C_{22}^2 - C_{12}^2)/C_{22}$, which are found to be 131.63 and 75.11 N/m, respectively. The Poisson's ratios of $\nu_a = C_{12}/C_{11} = 0.20$ and $\nu_b = C_{12}/C_{22} = 0.33$ are obtained accordingly. It is interesting to note that the in-plane Young's modulus E_a (131.63 N/m) is comparable to that of α -2D silica (131.78 N/m) [32], while E_b (75.11 N/m) is close to that of experimentally synthesized silicene (62 N/m) [39]. This can be explained by the structure characteristics of Orth-SiO: the Si-O bonds only exist in the x direction, while the Si-Si bonds are mainly along the y direction. Through the electron localization function (ELF) of two representative slices of Orth-SiO (see Fig. S1 in the Support Information (SI)), we find that the Si-Si bonds are covalent bonds, while the Si-O bonds exhibit ionic bond characteristics. Compared to the Si-Si bond, the Si-O bond is stronger, leading to the larger in-plane Young's modulus along the x direction. Moreover, with the decreased Si/O ratio, the

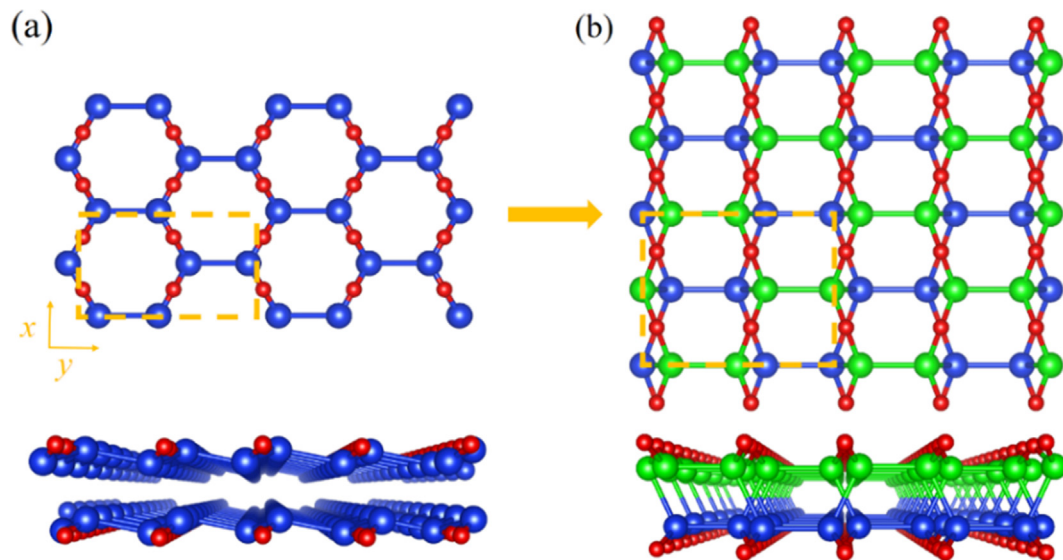


Fig. 3. (a) Top and side views of the initial structure. (b) Optimized structure with Orth-SiO configuration. The upper layer silicon atoms are in green. (For interpretation of the references to colour in this figure legend, the reader is referred to the web version of this article.)

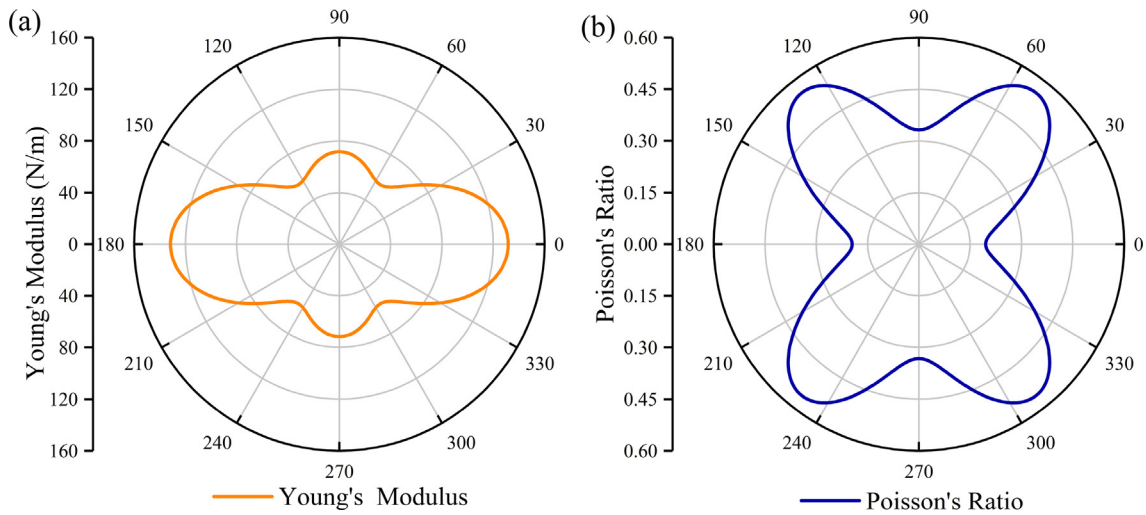


Fig. 4. Polar diagram for (a) Young's modulus and (b) Poisson's ratio of Orth-SiO.

number of Si-O bonds in a unit cell increases and the structures become stiffer, which is in consistent with the increased in-plane Young's modulus.

We further compute the Young's modulus (E) and Poisson's ratio (ν) along an arbitrary direction θ (θ is the angle relative to the x direction) using the following formulas:

$$E(\theta) = \frac{C_{11}C_{12} - C_{12}^2}{C_{11}s^4 + C_{22}c^4 + \left(\frac{C_{11}C_{12} - C_{12}^2}{C_{44}} - 2C_{12}\right)c^2s^2} \quad (1)$$

$$\nu(\theta) = \frac{\left(C_{11} + C_{22} - \frac{C_{11}C_{12} - C_{12}^2}{C_{44}}\right)c^2s^2 - C_{12}(c^4 + s^4)}{C_{11}s^4 + C_{22}c^4 + \left(\frac{C_{11}C_{12} - C_{12}^2}{C_{44}} - 2C_{12}\right)c^2s^2} \quad (2)$$

where $c = \cos \theta$ and $s = \sin \theta$ [40]. The calculated results are plotted in Fig. 4. One can see that the in-plane Young's modulus of Orth-SiO reaches its maximum in the (1 0 0) direction (0°) and minimum near the (1 1 0) direction ($\sim 55^\circ$), while the Poisson's ratio achieves its maximum near the (1 1 0) direction ($\sim 52^\circ$) and minimum in the (1 0 0) direction. As compared to the conventional 2D nanomaterials such as graphene, BN, especially the isotropic α -2D silica and planar silicene with hexagonal crystal structures, these results show the significant mechanical anisotropy in Orth-SiO, which attributes to its orthorhombic lattice, and the exhibited in-plane anisotropy may have potential applications in devices [41].

3.3. Electronic properties

To investigate the electronic properties of Orth-SiO, we calculate its electronic band structure at the PBE level and plot the result in Fig. 5(a). The band structure shows that Orth-SiO is semiconducting with a direct band gap of 0.76 eV since both the valence band maximum (VBM) and the conduction band minimum (CBM) are located at the Γ point. Considering the fact that most of the silicon and silicon dioxide materials are indirect band gap semiconductors or insulators, such direct band gap semiconductor may have potential applications in optical devices. To obtain a more accurate band gap, we recalculate the band structure by using the HSE06 functional. The results are also plotted in Fig. 5(a). The band structure calculated at the HSE06 level shows a similar band dispersion to that obtained at the PBE level. However, at the HSE06 level, the CBM is up-shifted, while the VBM makes almost no change, resulting in a wider band gap of 1.52 eV.

We also calculate the corresponding partial density of states (DOS) at the HSE06 level as displayed in Fig. 5(a), which shows that the VBM

is mainly contributed from the p_y orbitals of Si and O atoms, while the CBM is dominated by the p_z orbitals of O atoms. This is consistent with the partial charge densities of VBM and CBM shown in Fig. 5(b) and (c). The VBM mainly comes from the Si-Si bonding states along the y direction and in-plane O p_y orbitals parallel to them, while the CBM is contributed by the out-of-plane O p_z orbitals. This suggests that Orth-SiO possesses anisotropic electronic structure and may have a significant impact on the transport properties.

It is interesting to note that the ground state structure of 2D silicon dioxide, α -2D silica, is an insulator with a band gap of 7.31 eV [32], while the low buckled (LB) silicene shows metallic behavior [42]. To better understand the electronic properties of these silicon-based materials, we summarize the silicon bonding modes and show their electronic band structures and orbital-weighted electronic band structures in Fig. S2 for comparison. The three-fold coordinated Si atoms adopt mix sp^2 - sp^3 hybridization in LB-silicene [42], and the Si atoms are bonded to two Si and two O atoms with four-fold coordination in Orth-SiO while the all Si atoms are bonded to four O atoms with perfect sp^3 hybridization in α -2D silica [32]. Different hybridizations lead to different band gaps in these silicon-based structures. As shown Fig. S2, the valence and conduction bands near the Fermi level in LB-silicene are mainly contributed from the p_z orbitals of Si atoms, namely, π (Si-Si) bonds; The VBM of α -2D silica is contributed by the $2p$ orbitals of O atoms, and the CBM is mainly contributed from the $2s$ orbitals of O atoms. These results reveal that the involvement of the more electronegative O atoms broaden the band gap and the band gap of silicon-based materials is related to the Si/O ratio and the hybridization form of Si atoms.

We next investigate the carrier mobility of electrons and holes by using the Boltzmann transport equation with the deformation potential (DP) [43]. In 2D materials, the formula of carrier mobility along a given transport direction d can be written as

$$\mu_d = \frac{2e\hbar^3 C_{2D}}{3k_B T m_d^* m_e^* E_1^2} \quad (3)$$

where C_{2D} is the in-plane elastic constant and E_1 is the deformation potential constant under uniaxial strain along d direction [44]. According to the symmetry of Orth-SiO, the transport directions along the (1 0 0) and (0 1 0) are considered, and the C_{2D} is set as C_{11} and C_{22} , respectively. m_d^* is the effective mass of carriers in the direction d , and can be calculated by using the formula: $m_d^* = \hbar [\partial^2 E / \partial k^2]^{-1}$. We can get m_d^* by a quadratic polynomial fitting of the conduction and valence bands and $m_e^* = \sqrt{m_a^* m_b^*}$ is the mean effective mass. The calculated results of Orth-SiO are summarized in Table 2. One can see that both the effective mass and deformation potential constant exhibit strong

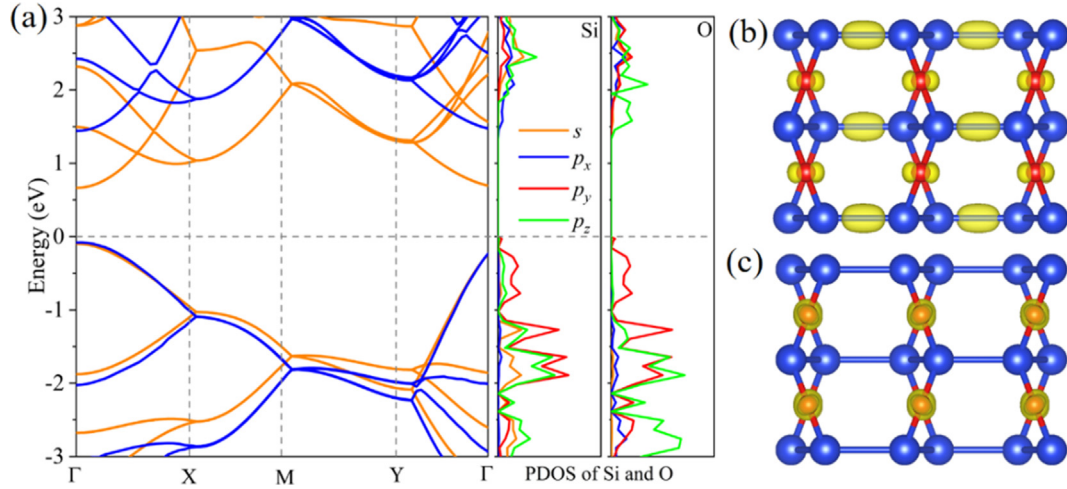


Fig. 5. (a) Electronic band structures of Orth-SiO at the PBE (orange lines) and HSE06 level (blue lines), and partial DOS of Orth-SiO at the HSE06 level. The Fermi level is shifted to 0 eV. Partial charge density for (b) the VBM and (c) CBM of Orth-SiO. (For interpretation of the references to colour in this figure legend, the reader is referred to the web version of this article.)

Table 2

In-plane elastic constant C_{2D} (in N/m), deformation potential constant E_1 (in eV), effective mass m_d^* (in m_e), and carrier mobility μ_d (in $\text{cm}^2 \cdot \text{V}^{-1} \cdot \text{s}^{-1}$) along the (1 0 0) and (0 1 0) directions for electrons and holes of Orth-SiO at 300 K.

Transport direction	carrier type	C_{2D}	E_1	m_d^*	μ_d
(1 0 0)	hole	136.84	0.62	1.03	8502.92
(1 0 0)	electron	136.84	11.20	0.70	23.03
(0 1 0)	hole	80.41	4.48	0.27	401.24
(0 1 0)	electron	80.41	1.15	1.33	675.63

anisotropies. The effective mass of holes in the x direction is much heavier than that in the y direction, while the effective mass of electrons exhibits opposite results. The low deformation potential of VBM under the strain along the x direction E_1 , together with the high in-plane elastic constant C_{11} , result in a high hole mobility of $8.5 \times 10^3 \text{ cm}^2 \cdot \text{V}^{-1} \cdot \text{s}^{-1}$ at 300 K, which is much higher than the values reported for other 2D semiconductors at the same temperature, such as $690 \text{ cm}^2 \cdot \text{V}^{-1} \cdot \text{s}^{-1}$ for WS_2 [45], $410 \text{ cm}^2 \cdot \text{V}^{-1} \cdot \text{s}^{-1}$ for MoS_2 [46] and $180 \text{ cm}^2 \cdot \text{V}^{-1} \cdot \text{s}^{-1}$ for MoSe_2 [45], indicating the potential applications of Orth-SiO in electronic devices.

3.4. Optical properties

The optical properties are determined by the complex dielectric function $\varepsilon(\omega) = \varepsilon_1(\omega) + i\varepsilon_2(\omega)$, and all frequency dependent optical constants can be deduced from the real part $\varepsilon_1(\omega)$ and imaginary part $\varepsilon_2(\omega)$ of dielectric function. Specifically, the absorption coefficient $I(\omega)$, the reflectivity $R(\omega)$ and the refraction index $n(\omega)$ are expressed as:

$$I(\omega) = \sqrt{2} [\sqrt{\varepsilon_1(\omega)^2 + \varepsilon_2(\omega)^2} - \varepsilon_1(\omega)]^{\frac{1}{2}} \quad (4)$$

$$R(\omega) = \left| \frac{\sqrt{\varepsilon(\omega)} - 1}{\sqrt{\varepsilon(\omega)} + 1} \right|^2 \quad (5)$$

$$\text{and } n(\omega) = \frac{\sqrt{2}}{2} [\sqrt{\varepsilon_1(\omega)^2 + \varepsilon_2(\omega)^2} + \varepsilon_1(\omega)]^{\frac{1}{2}} \quad (6)$$

Considering the anisotropy of Orth-SiO, we separately calculate these parameters along the xx and yy directions. all the results are plotted in Fig. 6. We only consider frequencies lower than 5 eV because they approximately cover the visible spectra. We divide this part into three regions: infrared region (0–1.63 eV), visible region (VIS) (1.63–3.27 eV) and ultraviolet region (UV) (3.27–5.00 eV). The

imaginary part of dielectric function $\varepsilon_2(\omega)$ is shown in Fig. 6(a), which describes absorption derived by the optical transitions between occupied and unoccupied bands. Since the band gap of Orth-SiO is 1.52 eV, Orth-SiO can only absorb phonons with energy > 1.52 eV. As we can see from Fig. 6(a), $\varepsilon_2(\omega)$ has a negligible value for photons with less than ~ 3 eV, indicating that little transition can occur under such stimulation. For the xx direction, the curve shows a sharp increase at about 4.3 eV and two peaks in $\varepsilon_2(\omega)$ at around 4.3 eV and 4.8 eV be well explained by the onsets of DOS. The two peaks in the range of 4.30–5.00 eV are mainly attributed to the transitions between Si-3p + O-2p valence bands to O-2p conduction bands. The absorption coefficient $I(\omega)$ is somehow similar to the imaginary part $\varepsilon_2(\omega)$. As shown in Fig. 6(b), the absorption coefficient $I(\omega)$ has a negligible value in the infrared and visible region, indicating that little transition can occur under such stimulation and Orth-SiO is an ideal transparent material. When the stimulation energy exceeds 4 eV, $I(\omega)$ increases quickly. However, $I(\omega)$ shows a significant anisotropy, especially in the UV region. Along the yy direction, strong absorption coefficient is observed in the UV region and reaches a maximum value of $\sim 4 \times 10^5 \text{ cm}^{-1}$, while along the xx direction, only little light is absorbed. This significant anisotropy of the absorption coefficient along the xx and yy directions indicates that Orth-SiO is a promising polarization filter in the UV region. Fig. 6(c) shows that the reflectivity spectra of Orth-SiO have a similar trend with the absorption spectra and also displays high anisotropy. In the range of 0.00–4.87 eV, the reflectivity in the xx direction is larger than that of the yy direction. As shown in Fig. 6(d), the refraction index reaches a high peak in the yy direction within the UV region, indicating the significant dispersion. From the above analyses, we find that Orth-SiO possesses anisotropic optical properties, which is suitable for wave plate, polarization microscope, and other polarization-sensitive devices.

3.5. Thermal properties

The specific heat capacity C_v at constant volume of Orth-SiO versus temperature is plotted in Fig. 7(a), from which one can see that the C_v increases rapidly with temperature when $T < 300$ K, following the Debye temperature rule as $C_v \propto T^3$ [47], while C_v approaches the classical Dulong-Petit limit ($3Nk_B$) [48,49] at high temperature. The specific heat capacity of Orth-SiO is larger than that of many other 2D materials at room temperature (300 K), including black phosphorus ($31.79 \text{ J} \cdot \text{K}^{-1} \cdot \text{mol}^{-1}$) [48], Ψ -graphene ($24.76 \text{ J} \cdot \text{K}^{-1} \cdot \text{mol}^{-1}$) [50] and graphene ($8.75 \text{ J} \cdot \text{K}^{-1} \cdot \text{mol}^{-1}$) [51]. Such a high specific heat capacity is beneficial for thermal energy storage [52,53].

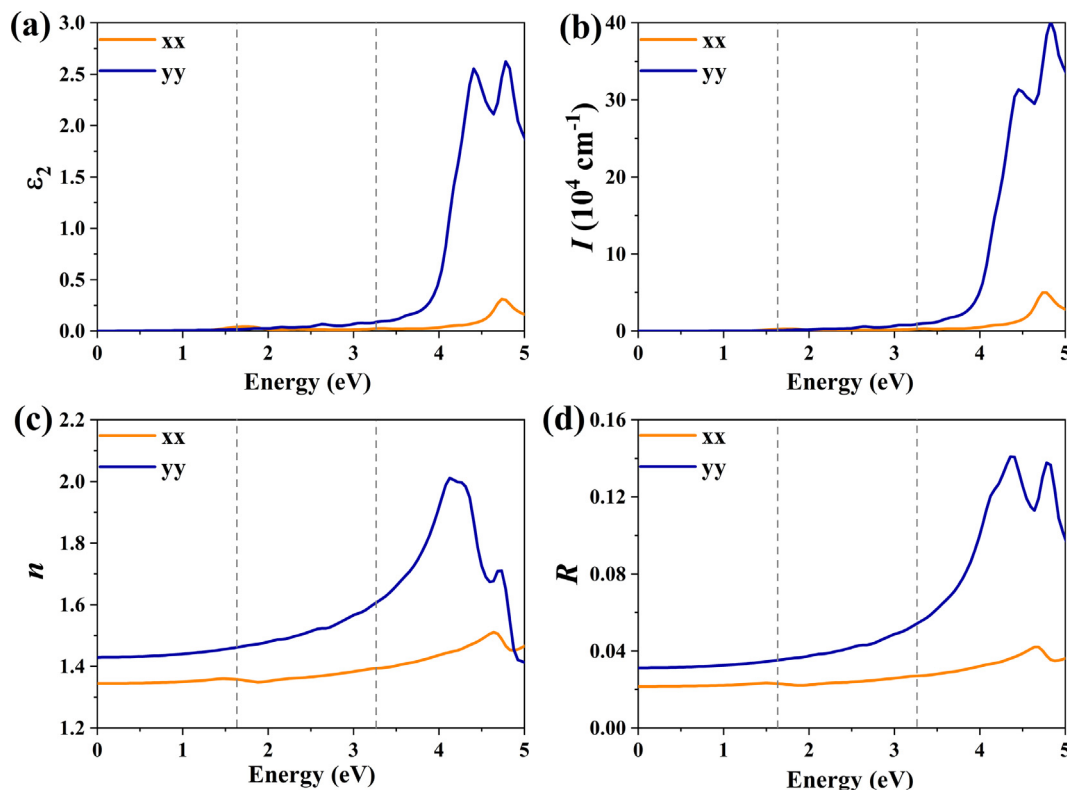


Fig. 6. (a) Optical absorption $\epsilon_2(\omega)$, (b) absorption coefficient $I(\omega)$, (c) refraction index $n(\omega)$, and (d) reflectivity $R(\omega)$ of Orth-SiO.

Since Orth-SiO is a semiconductor, phonons are the major heat carriers, then we focus on the lattice thermal conductivity (k_{lat}) of Orth-SiO, which can be calculated using ShengBTE code. The temperature dependence of k_{lat} is presented in Fig. 7(b). At room temperature k_{lat} is found to be 80.45 and 33.79 W/mK along the x and y directions, respectively, and k_{lat} decreases rapidly in $1/T$ when the temperature increases, indicating that anharmonic phonon-phonon interactions are dominant in the phonon scattering mechanism. Besides, the intrinsic lattice thermal conductivity is not only anisotropic but also much higher than that of many silicon-based materials including bulk crystal α -quartz (3.52 and 5.15 W/mK) [54], amorphous silica (1.7 W/mK) [54], large honeycomb dumbbell (LHD) silicene (5.9 W/mK) [55], dumbbell (DB) silicene (2.86 W/mK) [56] and LB-silicene (27.72 W/mK) [56], indicating that Orth-SiO is able to dissipate heat more efficiently in electronic devices. To further understand the origin of the large lattice thermal conductivity of the Orth-SiO sheet, the group velocity (V_g) and mode Grüneisen parameter (γ) are calculated, and their variations with frequency are plotted in Fig. 7(c) and (d), respectively. We note that the group velocity is higher than that of LB-silicene and DB-silicene [56], indicating faster energy propagation in the wave packets in Orth-SiO. Moreover, the optical branches show non-zero group velocities, comparable to those of the acoustic branches and in agreement with the phonon spectrum, while the Grüneisen parameter is smaller than that of LB-silicene and DB-silicene [56], indicating weaker anharmonicity in Orth-SiO. These factors together result in the large lattice thermal conductivity of the sheet.

4. Conclusions

In summary, on the basis of first principles calculations combined with the global structure search method, for the first time we have identified the ground state structure of 2D SiO sheet, Orth-SiO, which is not only energetically most stable among all the 2D SiO allotropes, but also dynamically, thermally, and mechanically stable. Band structure calculations reveal that Orth-SiO is semiconducting with a direct band

gap of 1.52 eV, which is very different from the semi-metallic silicene and insulating α -2D silica that has a wide band gap of 7.31 eV. By solving the Boltzmann transport equation, we have found that Orth-SiO possesses a high hole mobility of $8.5 \times 10^3 \text{ cm}^2 \cdot \text{V}^{-1} \cdot \text{s}^{-1}$ along the x direction due to the low deformation potential of the VBM and high in-plane elastic constant. The calculation of optical properties shows that Orth-SiO is transparent to visible light while showing strong absorption in UV region. Moreover, the lattice thermal conductivity of Orth-SiO at room temperature along the x and y direction is 80.45 and 33.79 W/mK, respectively, which is larger than that of bulk crystal α -quartz, amorphous silica, LHD-silicene, DB-silicene and LB-silicene because of its higher group velocity and smaller Grüneisen parameter resulting from the strong bonding in the geometry. These findings suggest that the silicon monoxide Orth-SiO sheet deserves experimental effort in synthesis for device applications.

Declaration of Competing Interest

There are no conflicts to declare.

CRediT authorship contribution statement

Yanyan Chen: Conceptualization, Writing - original draft, Methodology, Software, Formal analysis, Investigation, Data curation, Visualization. **Yupeng Shen:** Conceptualization, Methodology, Software, Formal analysis, Investigation, Data curation, Writing - review & editing, Visualization. **Yiheng Shen:** Methodology, Formal analysis, Investigation. **Xiaoyin Li:** Methodology, Software, Investigation. **Yaguang Guo:** Methodology, Software, Investigation. **Qian Wang:** Conceptualization, Funding acquisition, Project administration, Software, Writing - review & editing, Validation, Resources, Supervision.

Acknowledgements

This work is partially supported by grants from the National Natural Science Foundation of China (Grant Nos. 21773004 and 11974028), the

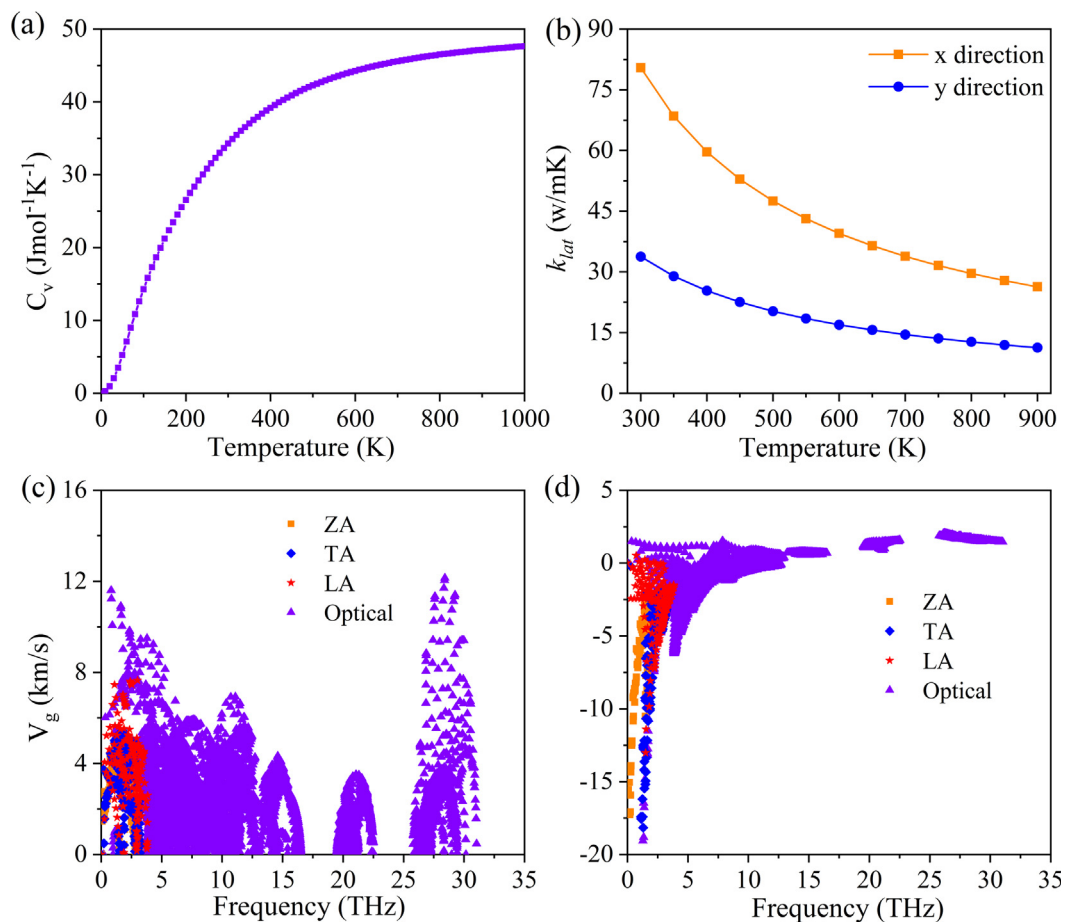


Fig. 7. Variation of (a) the constant volume specific heat capacity C_v , and (b) thermal conductivity k_{lat} with temperature, and (c) the group velocity V_g and (d) Grüneisen parameter γ with frequency of Orth-SiO.

National Key Research and Development Program of the Ministry of Science and Technology of China (Grants No. 2016YFE0127300 and 2017YFA0205003), and is supported by the High Performance Computing Platform of Peking University, China.

Appendix A. Supplementary data

Supplementary data to this article can be found online at <https://doi.org/10.1016/j.apsusc.2020.146759>.

References

- [1] I. Cherkneff, The chemistry of dust formation in red supergiants, EAS Publications Series (2013).
- [2] G. Kurdyumov, V. Molochko, A. Chekunov, Some Properties of Silicon Monoxide, *Izv. Akad. Nauk SSSR, Neorg. Mater* 8 (1966) 10–12.
- [3] V. Belot, R. Corriu, D. Leclercq, P. Lefevre, P. Mutin, A. Vioux, A. Flank, Sol-gel route to silicon suboxides. preparation and characterization of silicon sesquioxide, *J. Non-Cryst. Solids* 127 (1991) 207–214.
- [4] B. Gribov, K. Zinov'ev, O. Kalashnik, N. Gerasimenko, D. Smirnov, V. Sukhanov, Structure and phase composition of silicon monoxide, *Semiconductors* 46 (2012) 1576–1579.
- [5] R.Q. Zhang, W.J. Fan, Structures and properties of silicon oxide clusters by theoretical investigations, *J. Cluster Sci.* 17 (2006) 541–563.
- [6] Z. Liu, Q. Yu, Y. Zhao, R. He, M. Xu, S. Feng, S. Li, L. Zhou, L. Mai, Silicon oxides: a promising family of anode materials for lithium-ion batteries, *Chem. Soc. Rev.* 48 (2019) 285–309.
- [7] A. Prasad, S. Balakrishnan, S.K. Jain, G.C. Jain, Porous silicon-oxide antireflection coating for solid-cells, *J. Electrochem. Soc.* 129 (1982) 596–599.
- [8] A. Hirata, S. Kohara, T. Asada, M. Arai, C. Yogi, H. Imai, Y. Tan, T. Fujita, M. Chen, Atomic-scale disproportionation in amorphous silicon monoxide, *Nat. Commun.* 7 (2016) 11591.
- [9] K. Yasuda, Y. Kashitani, S. Kizaki, K. Takeshita, T. Fujita, S. Shimozaki, Thermodynamic analysis and effect of crystallinity for silicon monoxide negative electrode for lithium ion batteries, *J. Power Sources* 329 (2016) 462–472.
- [10] K. AlKaabi, D.L.V.K. Prasad, P. Kroll, N.W. Ashcroft, R. Hoffmann, Silicon monoxide at 1 atm and elevated pressures: crystalline or amorphous? *J. Am. Chem. Soc.* 136 (2014) 3410–3423.
- [11] S.M. Schnurre, J. Gröbner, R. Schmid-Fetzer, Thermodynamics and phase stability in the Si–O system, *J. Non-Cryst. Solids* 336 (2004) 1–25.
- [12] S.S. Batsanov, Optical properties and structure of silicon monoxide, *Russ. J. Phys. Chem. A* 90 (2016) 250–251.
- [13] S. Mankefors, T.G. Andersson, I. Panas, Possible metallicity in SiO and GeO solids, *Chem. Phys. Lett.* 322 (2000) 166–174.
- [14] Y. Wang, D. Yi, Mechanical and electronic properties of stoichiometric silicene and germanene oxides from first-principles, *Phys. Status Solidi RRL* 7 (2013) 410–413.
- [15] Y. Wang, J. Lv, L. Zhu, Y. Ma, Crystal structure prediction via particle-swarm optimization, *Phys. Rev. B* 82 (2010) 094116.
- [16] Y. Wang, J. Lv, L. Zhu, Y. Ma, CALYPSO: a method for crystal structure prediction, *Comput. Phys. Commun.* 183 (2012) 2063–2070.
- [17] D. Löffler, J.J. Uhlrich, M. Baron, B. Yang, X. Yu, L. Lichtenstein, L. Heinke, C. Büchner, M. Heyde, S. Shaikhutdinov, Growth and structure of crystalline silica sheet on Ru(0001), *Phys. Rev. Lett.* 105 (2010) 146104.
- [18] T.K. Todorova, M. Sierka, J. Sauer, S. Kaya, J. Weissenrieder, J.-L. Lu, H.-J. Gao, S. Shaikhutdinov, H.-J. Freund, Atomic structure of a thin silica film on a Mo(112) substrate: a combined experimental and theoretical study, *Phys. Rev. B* 73 (2006) 165414.
- [19] G. Kresse, J. Furthmüller, Efficient iterative schemes for ab initio total-energy calculations using a plane-wave basis set, *Phys. Rev. B* 54 (1996) 11169.
- [20] P.E. Blöchl, Projector augmented-wave method, *Phys. Rev. B: Condens. Matter Mater. Phys.* 50 (1994) 17953–17979.
- [21] G. Kresse, D. Joubert, From ultrasoft pseudopotentials to the projector augmented-wave method, *Phys. Rev. B* 59 (1999) 1758–1775.
- [22] J.P. Perdew, K. Burke, M. Ernzerhof, Generalized gradient approximation made simple, *Phys. Rev. Lett.* 77 (1996) 3865–3868.
- [23] Y. Liu, C. Storey, Efficient generalized conjugate gradient algorithms, part 1: theory, *J. Optim. Theory Appl.* 69 (1991) 139–152.
- [24] J. Paier, M. Marsman, K. Hummer, G. Kresse, I.C. Gerber, J.G. Ángyán, Screened hybrid density functionals applied to solids, *J. Chem. Phys.* 124 (2006) 154709.
- [25] J. Heyd, G.E. Scuseria, M. Ernzerhof, Erratum: “Hybrid Functionals Based on a Screened Coulomb Potential” [*J. Chem. Phys.* 118, 8207 (2003)], *J. Chem. Phys.* 124 (2006) 219906.

- [26] H.J. Monkhorst, J.D. Pack, Special points for brillouin-zone integrations, *Phys. Rev. B* 13 (1976) 5188.
- [27] M. Omini, A. Sparavigna, An iterative approach to the phonon boltzmann equation in the theory of thermal conductivity, *Phys. B* 212 (1995) 101–112.
- [28] W. Li, J. Carrete, N.A. Katcho, N. Mingo, ShengBTE: a solver of the boltzmann transport equation for phonons, *Comput. Phys. Commun.* 185 (2014) 1747–1758.
- [29] A. Togo, I. Tanaka, First principles phonon calculations in materials science, *Scr. Mater.* 108 (2015) 1–5.
- [30] K. Parlinski, Z.Q. Li, Y. Kawazoe, First-principles determination of the soft mode in cubic, *Phys. Rev. Lett.* 78 (1997) 4063–4066.
- [31] R. Wang, X. Pi, Z. Ni, Y. Liu, S. Lin, M. Xu, D. Yang, Silicene oxides: formation, structures and electronic properties, *Sci. Rep.* 3 (2013) 3507.
- [32] Z. Gao, X. Dong, N. Li, J. Ren, Novel two-dimensional silicon dioxide with in-plane negative poisson's ratio, *Nano Lett.* 17 (2017) 772–777.
- [33] G. Wang, G.C. Loh, R. Pandey, S.P. Karna, Novel two-dimensional silica monolayers with tetrahedral and octahedral configurations, *J. Phys. Chem. C* 119 (2015) 15654–15660.
- [34] Y.L. Page, P. Saxe, Symmetry-general least-squares extraction of elastic data for strained materials from ab initio calculations of stress, *Phys. Rev. B* 65 (2002) 104104.
- [35] Z. Wu, E. Zhao, H. Xiang, X. Hao, X. Liu, J. Meng, Crystal structures and elastic properties of superhard IrN_2 and IrN_3 from first principles, *Phys. Rev. B* 76 (2007) 054115.
- [36] Y. Du, J. Zhuang, H. Liu, X. Xu, S. Eilers, K. Wu, P. Cheng, J. Zhao, X. Pi, K.W. See, Tuning the band gap in silicene by oxidation, *ACS Nano* 8 (2014) 10019–10025.
- [37] X. Xu, J. Zhuang, Y. Du, H. Feng, N. Zhang, C. Liu, T. Lei, J. Wang, M. Spencer, T. Morishita, Effects of oxygen adsorption on the surface state of epitaxial silicene on $\text{Ag}(111)$, *Sci. Rep.* 4 (2014) 7543.
- [38] J. Zhuang, X. Xu, H. Feng, Z. Li, X. Wang, Y. Du, Honeycomb silicon: a review of silicene, *Sci. Bull.* 60 (2015) 1551–1562.
- [39] D. Yi, W. Yanli, Density functional theory study of the silicene-like SiX and XS_3 ($X = \text{B}, \text{C}, \text{N}, \text{Al}, \text{P}$) honeycomb lattices: the various buckled structures and versatile electronic properties, *J. Phys. Chem. C* 117 (2013) 18266–18278.
- [40] E. Cadelano, P.L. Palla, S. Giordano, L. Colombo, Elastic properties of hydrogenated graphene, *Phys. Rev. B* 82 (2010) 235414.
- [41] L. Li, P. Gong, W. Wang, B. Deng, L. Pi, J. Yu, X. Zhou, X. Shi, H. Li, T. Zhai, Strong in-plane anisotropies of optical and electrical response in layered dimetal chalcogenide, *ACS Nano* 11 (2017) 10264–10272.
- [42] F. Matusalem, M. Marques, L.K. Teles, F. Bechstedt, Stability and electronic structure of two-dimensional allotropes of group-IV materials, *Phys. Rev. B* 92 (2015) 045436.
- [43] J. Bardeen, W. Shockley, Deformation potentials and mobilities in non-polar crystals, *Phys. Rev.* 80 (1950) 72–80.
- [44] J. Qiao, X. Kong, Z.X. Hu, F. Yang, W. Ji, High-mobility transport anisotropy and linear dichroism in few-layer black phosphorus, *Nat. Commun.* 5 (2014) 4475.
- [45] Z. Jin, X. Li, J.T. Mullen, K.W. Kim, Intrinsic transport properties of electrons and holes in monolayer transition metal dichalcogenides, *Phys.* 90 (2014) 55–58.
- [46] K. Kaasbjerg, K.S. Thygesen, K.W. Jacobsen, Phonon-limited mobility in n-type single-layer MoS_2 from first principles, *Phys. Rev. B* 85 (2012) 115317.
- [47] B. Sabir, G. Murtaza, R.M. Arif Khalil, Q. Mahmood, First principle study of electronic, mechanical, optical and thermoelectric properties of CsMO_3 ($M = \text{Ta}, \text{Nb}$) compounds for optoelectronic devices, *J. Mol. Graph. Model.* 86 (2019) 19–26.
- [48] C.E. Ekuma, S. Najmaei, M. Dubey, Electronic and vibrational properties of van der waals heterostructures of vertically stacked few-layer atomically thin MoS_2 and BP , *Mater. Today Commun.* 19 (2019) 383–392.
- [49] H. Sun, G. Liu, Q. Li, X.G. Wan, First-principles study of thermal expansion and thermomechanics of single-layer black and blue phosphorus, *Phys. Lett. A* 380 (2016) 2098–2104.
- [50] S. Thomas, E.B. Nam, S.U. Lee, Atomistic dynamics investigation of the thermo-mechanical properties and li diffusion kinetics in ψ -graphene for LIB anode material, *ACS Appl. Mater. Interfaces* 10 (2018) 36240–36248.
- [51] F. Ma, H.B. Zheng, Y.J. Sun, D. Yang, K.W. Xu, P.K. Chu, Strain effect on lattice vibration, heat capacity, and thermal conductivity of graphene, *Appl. Phys. Lett.* 101 (2012) 111904.
- [52] F. Wang, W. Lin, Z. Ling, X. Fang, A comprehensive review on phase change material emulsions: fabrication, characteristics, and heat transfer performance, *Sol. Energy Mater. Sol. Cells* 191 (2019) 218–234.
- [53] M.E. Kilic, K.-R. Lee, Tuning the electronic, mechanical, thermal, and optical properties of tetrahexcarbon via hydrogenation, *Carbon* 161 (2020) 71–82.
- [54] Y. Han, G. Qin, C. Jungemann, M. Hu, Strain-modulated electronic and thermal transport properties of two-dimensional O-silica, *Nanotechnology* 27 (2016) 265706.
- [55] Y. Han, J. Dong, G. Qin, M. Hu, Phonon transport in the ground state of two-dimensional silicon and germanium, *RSC Adv.* 6 (2016) 69956–69965.
- [56] B. Peng, H. Zhang, H. Shao, Y. Xu, R. Zhang, H. Lu, D.W. Zhang, H. Zhu, First-principles prediction of ultralow lattice thermal conductivity of dumbbell silicene: a comparison with low-buckled silicene, *ACS Appl. Mater. Interfaces* 8 (2016) 20977–20985.